FULL-LENGTH PAPER

Structural hierarchy of mechanical extensibility in human von Willebrand factor multimers

Mária Csilla Csányi[1] | **Pál Salamon[1]** | **Tímea Feller[1]** | **Tamás Bozó[1]** | **Jolán Hársfalvi[1]** [ORCID] | **Miklós S. Z. Kellermayer[1]** [ORCID]

[1]Department of Biophysics and Radiation Biology, Semmelweis University, Budapest, Hungary

Correspondence
Miklós S. Z. Kellermayer and Jolán Hársfalvi, Department of Biophysics and Radiation Biology, Semmelweis University, Tűzoltó u. 37-47, Budapest H1094, Hungary.
Email: kellermayer.miklos@med.semmelweis-univ.hu and harsfalvi.jolan@med.semmelweis-univ.hu

Present address
Pál Salamon, Department of Bioengineering, Sapientia Hungarian University of Transylvania, Miercurea Ciuc, Romania.

Tímea Feller, Discovery and Translational Science Department, Leeds Institute of Cardiovascular and Metabolic Medicine, University of Leeds, Leeds, UK.

Review Editor: John Kuriyan

Abstract

The von Willebrand factor (VWF) is a multimeric glycoprotein composed of 80- to 120-nm-long protomeric units and plays a fundamental role in mediating platelet function at high shear. The exact nature of the shear-induced structural transitions have remained elusive; uncovering them requires the high-resolution quantitative analysis of gradually extended VWF. Here, we stretched human blood-plasma-derived VWF with molecular combing and analyzed the axial structure of the elongated multimers with atomic force microscopy. Protomers extended through structural intermediates that could be grouped into seven distinct topographical classes. Protomer extension thus progresses through the uncoiling of the C_{1-6} domain segment, rearrangements among the N-terminal VWF domains, and unfolding and elastic extension of the A_2 domain. The least and most extended protomer conformations were localized at the ends and the middle of the multimer, respectively, revealing an apparent necking phenomenon characteristic of plastic-material behavior. The structural hierarchy uncovered here is likely to provide a spatial control mechanism to the complex functions of VWF.

KEYWORDS
atomic force microscopy, conformation, receding meniscus, topography, VWF protomer

1 | INTRODUCTION

The von Willebrand factor (VWF) is an array of multimeric (concatameric), disulfide-linked, mirror-symmetric glycoprotein dimers called protomers (Springer, 2014). The mature VWF monomer is a 2050-residue protein (MW ~ 250 kDa) containing 12 N-linked and 10 O-linked oligosaccharide chains. Its most abundant amino
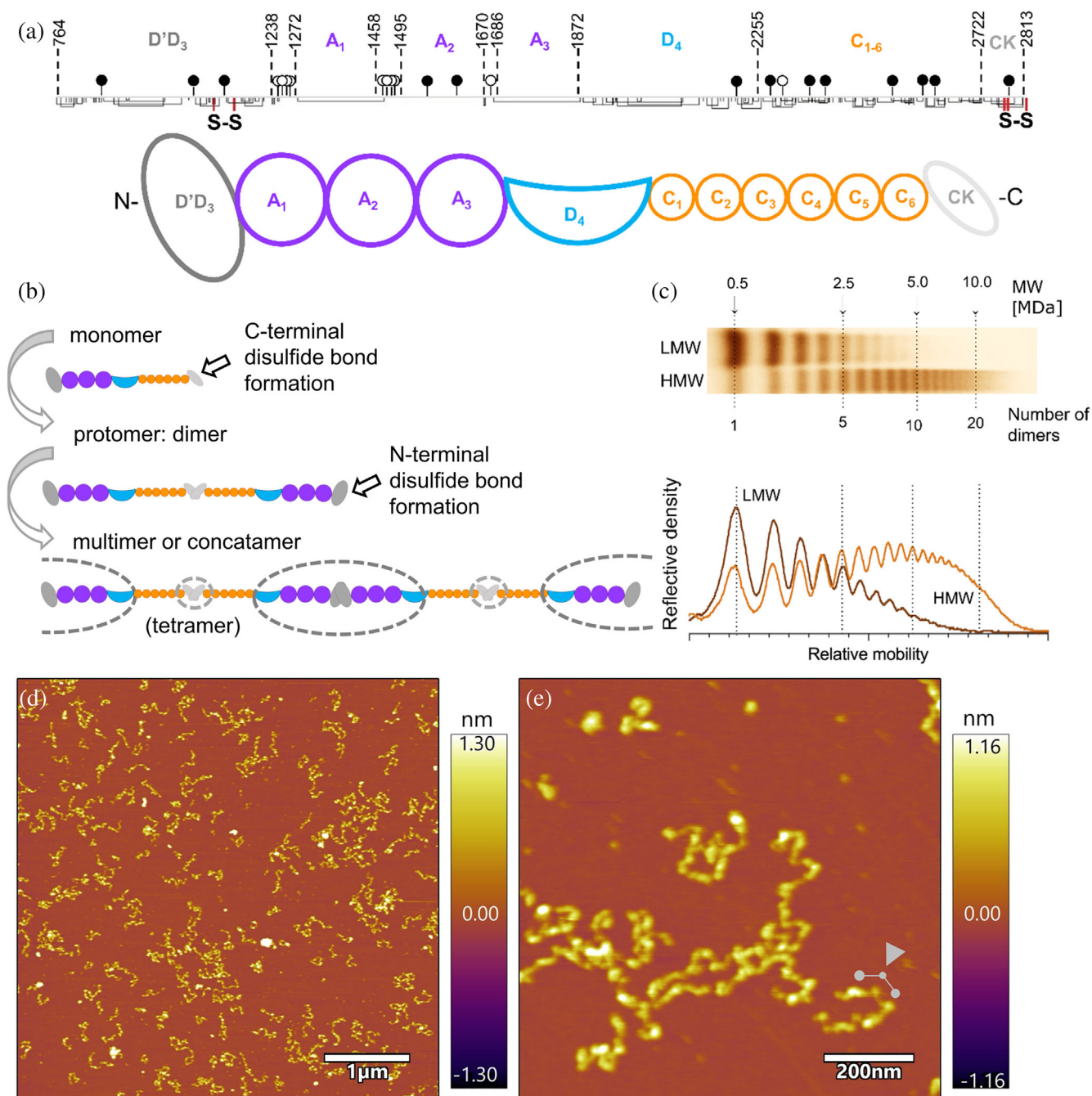
FIGURE 1 Schematics, electrophoresis, and AFM of the von Willebrand factor. (a) Domain structure of the mature VW monomer is shown in detail. For easier reference, in the present work we use a subscripted domain designation of $D'D_3A_1A_2A_3D_4C_{1-6}CK$ (instead of the usual $D'D_3A_1A_2A_3D_4C_1C_2C_3C_4C_5C_6CK$). Above the top line closed and open lollipops show N- and O-linked oligosaccharide chains, respectively. Numbers indicate the domain-bounding amino acid number along the full-length VWF. Below the line cysteines are vertical lines and are connected for disulfide bonds. (b) Schematic steps of VWF concatamerization. Dashed ellipses indicate structures identified as nodules in AFM images. (c) Electrophoretic pattern (top) and densitometric curve (bottom) of a VWF sample containing low (LMW) and high molecular weight (HMW) multimers. In this work, HMW fractions were analyzed. (d) Height-contrast AFM image of VWF multimers equilibrated to mica surface in relaxed conformation. (e) Enlarged view of conformationally relaxed VWF multimers. Gray arrowhead points at a $C_{1-6}(CK)_2C_{1-6}$ segment in the open conformation

acid is cysteine (8.3%). Numerous disulfide bonds and cysteine-rich sequences occur within domains and at flexible inter-domain junctions (Figure 1a). A_{1-3} are loop domains with hydrophobic cores. The loops in A_1 and A_3

are disulfide-linked. Every domain carries binding sites for specific functions. D' and D_3 bind factor VIII and present it to platelets. A_1 binds GPIbα (thereby initiating platelet rolling), heparin and collagen I. A_2 provides a

cleavage site for ADAMTS13 which regulates multimer size. A_3 binds collagens I and III, thus tethering VWF at sites of tissue injury. D_4 binds ADAMTS13. C_{1-6} domains bind the platelet receptor GPIIbIIIa (Bonazza et al., 2015; Fu et al., 2017; Lancellotti, Sacco, Basso, & Cristofaro, 2019; Zhou et al., 2012).

Multimer formation and glycosylation of VWF arise from extensive post-translational modifications. Tail-to-tail dimerization of monomers occurs via C-terminal cystine knot (CK) motifs in the endoplasmic reticulum of endothelial cells (ECs) and megakaryocytes. Dimers form a dimeric bouquet $[_N D' D_3 A_1 A_2 A_3 D_4 C_{1-6} (CK)_2 C_{1-6} D_4 A_3 A_2 A_1 D_3 D'_N]$ during synthesis, where $C_{1-6}(CK)_2 C_{1-6}$ is a stem that opens at physiological pH (Zhou et al., 2012). Head-to-head multimerization of dimers proceeds via the N-terminal D domains (Figure 1b) while assembling into helical tubules inside the Golgi apparatus and during transfer to storage pools (Weibel-Palade bodies of ECs, a-granules of platelets) from where a steady VWF secretion can be enhanced upon stimuli. Secreted VWFs containing more than 100 dimers are cleaved by proteases (ADAMTS13, plasmin, neutrophil elastase, and thrombin) if cleavage sites are exposed (De Ceunynck et al., 2011; Karampini, Bierings, & Voorberg, 2020; Wohner, Kovács, Machovich, & Kolev, 2012). Multimers in vivo contain 1–24 dimeric units and have a 12-h half-life in circulation (Parker & Lollar, 2021). VWF is a sensor of shear force in blood flow, and multimer length is key to its function. The multimer can be extended by shear stress (>1 N/m^2), which modulates VWF function in platelet-vessel-wall and platelet–platelet interactions by exposing local binding sites and forming tethers. Long tethers are extended more easily at a given shear stress than short ones (Fu et al., 2017; Lancellotti et al., 2019; Springer, 2014). Certain domains of VWF have been suggested to sense forces by extension ($C_{1-6}(CK)_2 C_{1-6}$) and unfolding (A_2) (Baldauf et al., 2009; Chen, Lou, & Zhu, 2009; Ying, Ling, Westfield, Sadler, & Shao, 2010; Zhang et al., 2009; Zhang, Halvorsen, Zhang, Wong, & Springer, 2009; Zhou et al., 2011).

Ever since electrophoresis of blood-plasma VWF revealed a ladder pattern suggesting concatamerization (Ruggeri & Zimmerman, 1981), VWF structure has been the subject of intense investigation. Electron microscopy (EM) revealed that the native VWF is a flexible, unbranched filament with a length and diameter of 50–2000 and 2–3 nm, respectively (Fowler, Fretto, Hamilton, Erickson, & McKee, 1985; Ohmori et al., 1982; Slayter, Loscalzo, Bockenstedt, & Handin, 1985). It is a beads-on-a-string structure, in which dimeric units, consisting of two large globular end domains embracing a small central nodule via two flexible rods, are axially linked (Fowler et al., 1985). Atomic force microscopy (AFM) has been used to explore extended VWF multimers (Bonazza et al., 2015; Eppell, Zypman, & Marchant, 1993; Marchant, Lea, Andrade, & Bockenstedt, 1992; Seyfried et al., 2010) and substantiated the EM observations (Bonazza et al., 2015; Siedlecki et al., 1996). At forces above $\sim$50 pN, a pH-dependent opening of the C-domain stem occurs, which provides $\sim$80 nm dimer length gain (Mueller et al., 2016). The effects of force on VWF's structure and interactions have been extensively studied with microfluidics (Fu et al., 2017), fluorescence (Fu et al., 2017; Wang et al., 2019), and optical tweezers (Zhang, Halvorsen, et al., 2009). Yet, our picture of how forces modulate global and local VWF conformation is far from complete due to the difficulty of combining a well-controlled nanomechanical environment with high-resolution structural methods.

Here, we investigated the topography of protomers within multimers, stretched to different lengths by molecular combing (Martonfalvi & Kellermayer, 2014; Shimanuki, Matsuta, Fujita, & Kumaki, 2018; Tskhovrebova & Trinick, 2001; Yokota, Sunwoo, Sarikaya, van den Engh, & Aebersold, 1999), to uncover and quantitatively characterize structural stages during VWF extension. Protomers extended via intermediates that could be partitioned into seven classes. Most of the extension was due to uncoiling of C_{1-6}, and the unfolding and subsequent extension of the A_2 domain. The least and most extended protomer conformers were localized in the ends and the middle of the multimer, respectively, pointing at an apparent plastic behavior of VWF. The structural hierarchy uncovered here is likely to provide a spatial control mechanism for the complex functions of VWF.

2 | RESULTS

2.1 | AFM imaging of VWF multimers

First, the topographical structure of conformationally relaxed VWF was explored with high-resolution AFM (Figure 1d,e). Multimers equilibrated on mica appeared as filamentous structures of various contour lengths displaying random-coil structure (Figure 1d). The variation in contour length reflected the wide size distribution of VWF in the HMW fraction (Figure 1c). In magnified AFM images (Figure 1e), the sub-filamentous structure of VWF became visible. The VWF multimers displayed a beads-on-a-string appearance, and often distinct nodules interconnected with thin segments could be resolved (Figure 1e, arrowhead). A fraction ($\sim$5%) of analyzed multimers ($n = 625$) contained partially or completely zippered dimers (Figure S1).
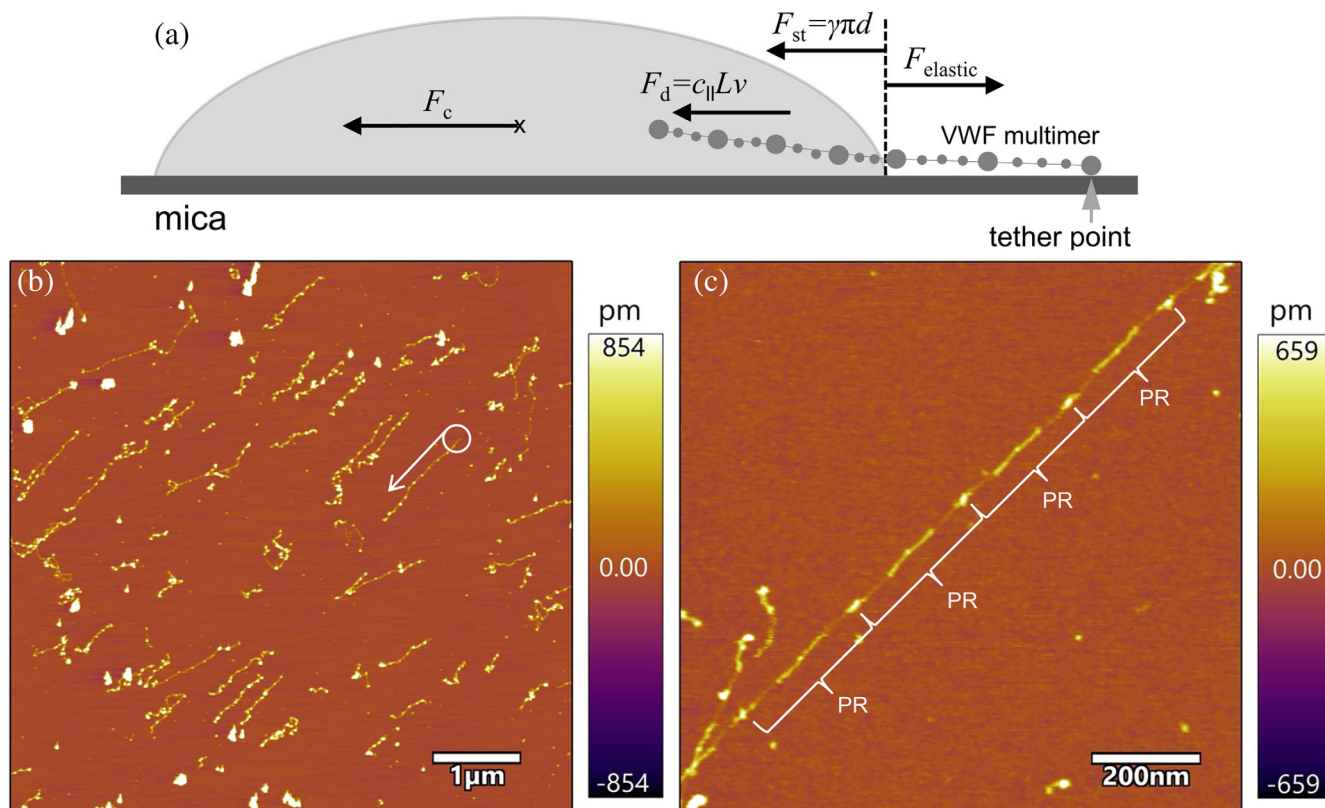
FIGURE 2 Molecular combing of VWF. (a) Schematics of stretching a VWF multimer with receding meniscus. Centrifugal force (F_c) accelerates the buffer droplet over the sample. Drag force (F_d) and surface-tension-based force (F_{st}) stretch the VWF multimer against its elasticity ($F_{elastic}$). Forces are indicated with arrows at the approximate points of attack: F_c at the center of mass of the droplet, F_d along the length of the VWF multimer in fluid, and F_{st} and $F_{elastic}$ on the multimer at the droplet edge. Adhesion force, which finally stabilizes the VWF multimer on the mica surface, is not shown. D is the average diameter of the VWF, γ is surface tension, $c_{\parallel}$ is the drag coefficient parallel with the long axis of the VWF multimer, L is VWF length and v is droplet velocity. (b) Height-contrast AFM image of VWF multimers stretched with receding meniscus. White circle and arrow point at the tether point and the direction of the fluid flow, respectively, for one of the VWF multimers. (c) Enlarged view of a stretched VWF multimer. The "PR" labels indicate the putative VWF protomers

2.2 | Mechanical stretching of VWF multimers

We then stretched VWF multimers with receding meniscus (Figure 2) which sequentially imposed shear-related drag (F_d) and surface-tension-based (F_{st}) forces on the multimer (Figure 2a). VWF multimers became oriented in the direction of the centrifugal force (F_c), and most of the filaments straightened out (Figure 2b). The magnified AFM image of a straightened VWF (Figure 2c) was reminiscent of the bead-on-a-string structure, but the nodules and the interconnecting segments appeared elongated. The filaments are partitioned into self-similar, repeating segments with a mirror-symmetric structure, which we identified as the differently extended VWF protomer (PR). To test whether the periodic structures indeed correspond to protomers, which are interconnected by disulfide bonds, we treated the meniscus-stretched VWF multimers with DTT (Figure 3). Increasing DTT

concentration resulted in increased fragmentation of the VWF multimer into progressively smaller structural units. Eventually, three-nodule fragments characteristic of contracted protomers appeared (Figure 3d).

2.3 | Analysis of protomer extension

To uncover the mechanical status of protomers in the meniscus-stretched VWF multimer, we carried out systematic measurements of protomer length (Figure 4). In a stretched multimer the protomer boundaries were identified as nodules with local topographical height maxima (Figure 4a). Hence, the distance between consecutive large nodules provided the protomer length. The multimer contour length was proportional to the number of constituent protomers (Figure 4b). However, the distribution of the data suggested a non-linear dependence indicating that the multimer contour is not simply the
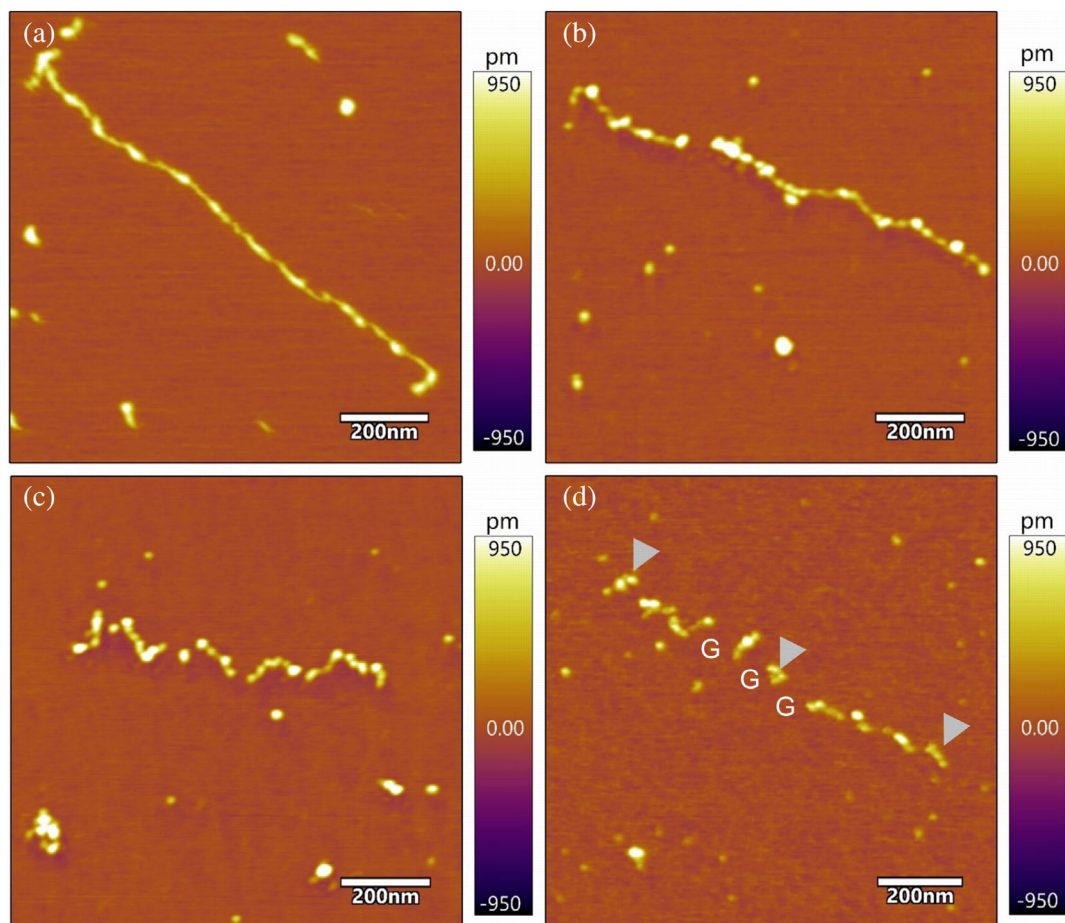
FIGURE 3 Effect of DTT on the structure of the stretched VWF multimer. (a) Control VWF (no DTT). VWF samples stretched with receding meniscus were treated, for 10 min, with 0.1 mM (b), 2 mM (c), and 20 mM (d) DTT before washing, drying and AFM scanning. Arrowheads point at single protomers with three interconnected nodes. Letters of "G" indicate topographical gaps along the VWF multimer

arithmetic sum of the protomer lengths, but protomer extension may also contribute to the overall multimer length. To test for this possibility, we calculated the average protomer length as a function of the multimer contour length (Figure 4c). In support of our hypothesis, the average protomer length was not constant but increased with increasing VWF multimer length. Direct measurement of protomer lengths gave an identical result (Figure 4d). The linear fits on the data shown in Figure 4c,d indicates that the resting length of a protomer is ∼54–62 nm, and protomer length increases by 4 nm for every 100 nm of multimer extension. In the longest VWF multimers, the protomer length often reached four times its resting length.

2.4 | Conformational classes of VWF protomers

The high-resolution AFM images made it possible to identify VWF domains based on which the protomers

could be assigned to structural classes (Figure 5). The image of a highly extended multimer (Figure 5a) and its axial height profile plot (Figure 5b) show the logic of domain identification and topographical nodule assignment. We identified seven classes of topographical conformation into which essentially all protomers could be assigned depending on the magnitude of the extension. The increasing protomer class number (from PR1 to PR7) corresponds to a gradually increasing extension. Examples of conformational classes (i.e., conformers) are shown in Figures 5c and S2, and the corresponding explanations are in Figure 5d,e and Table 1. Notably, the main conformers are mirror symmetric, but we also found asymmetric ones (Figure 5f).

2.5 | Structure and mechanics of VWF protomer conformers

To uncover the properties of the conformers and their role in VWF extensibility, we carried out detailed
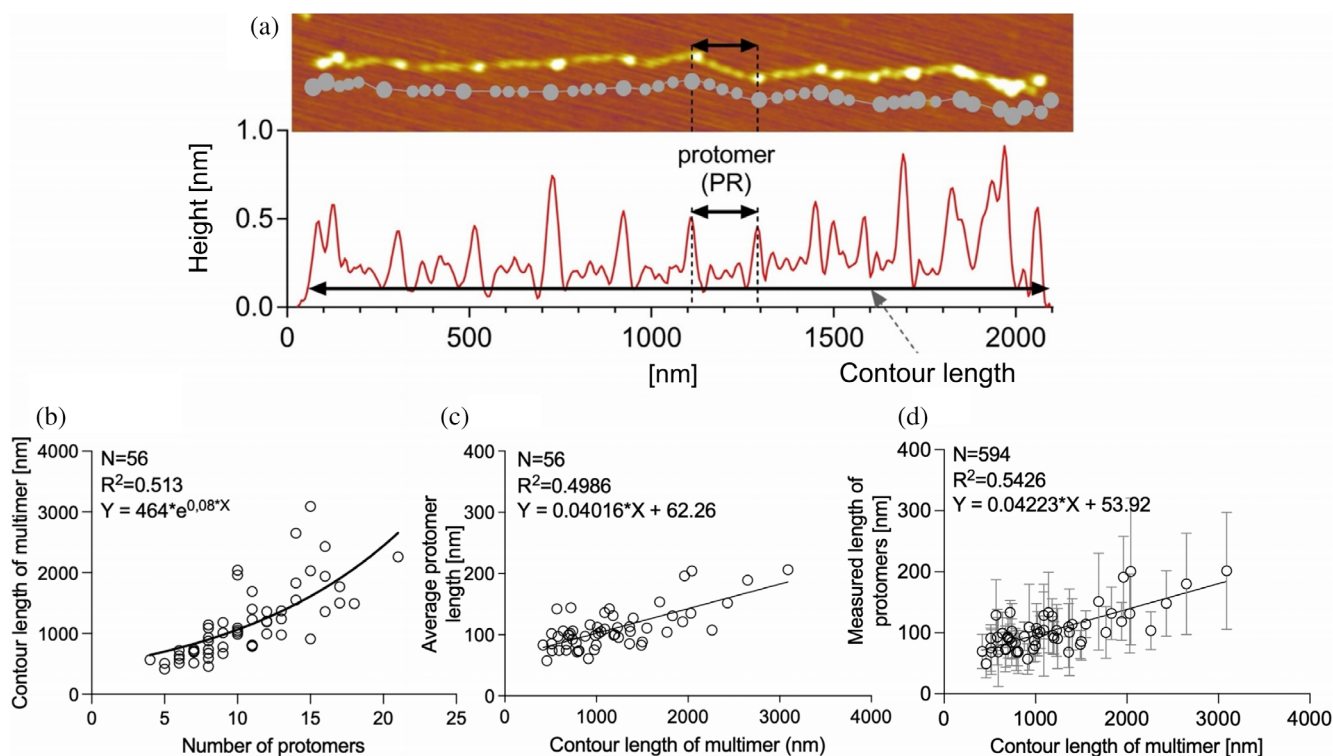
FIGURE 4 Analysis of protomer length in stretched VWF multimers. (a) Height-profile AFM image of a meniscus-stretched VWF multimer with an explanatory beads-on-a-string schematic model shown in gray (top). Topographical height profile plot obtained by manual tracking along the axis of the VWF multimer (bottom). Assuming that the large nodules (at local height maxima) are N-terminal junctions, the section between two consecutive large nodules is identified as the protomer (PR). (b) Contour length of the VWF multimer as a function of the number of protomers. (c) Average length of the protomer, calculated as the multimer contour length divided by protomer number, as a function of the contour length of the VWF multimer. (d) Length of the protomers, measured directly from the height profile plots, as a function of the contour length of the VWF multimer

analyses of topographical parameters (Figure 6, Table 2). The topographical height of all the three structural nodules (N-terminal, $(CK)_2$, A_3D_4) decreased progressively as a function of protomer length and conformational class (Figures 6a–c, S2), suggesting that structural rearrangements, most likely partial unfolding, took place in the respective constituent domains. Conformationally relaxed VWF multimers were dominated by the presence of PR1 and PR2 protomers (frequency 98.5%) containing large (N-terminal) nodules of similar topographical height (Table 2), and they were essentially devoid of higher-order extended protomers (PR3–PR7) in which small nodules (A_3D_4 and $(CK)_2$) are apparent. By contrast, in VWF multimers stretched with molecular combing the frequency of PR1 and PR2 was significantly reduced (43.5%) and higher-order protomers became prevalent.

To quantitatively assess the mechanistic contributors to protomer extension, we analyzed the end-to-end length distribution of the C_{1-6} segment and the A_2 domain. The C_{1-6} segment length histogram displayed a peak at $\sim$10 nm, and the statistical frequency was minimized above $\sim$35 nm (Figure 6d). The A_2 length was

distributed nearly continuously between 0 and 40 nm, then the statistical frequency decayed by 70 nm (Figure 6e). The A_2 domain end-to-end length at the half-maximal statistical frequency was $\sim$55 nm. Quite interestingly, while the length of the individual protomer classes appeared independent of their position within the multimer (Figure 6f), the distribution of the conformers was uneven along the multimer: short (PR1) and long (PR6, PR7) conformers populated the ends and the middle of the extended VWF multimer, respectively (Figures 6g–i and S3).

3 | DISCUSSION

In the present work, we mechanically manipulated native, high-molecular-weight (HMW) VWF multimers purified from human blood plasma and investigated their structural properties with high-resolution AFM and quantitative image analysis.

Conformationally relaxed multimers adsorbed to mica surface displayed a beads-on-a-string appearance
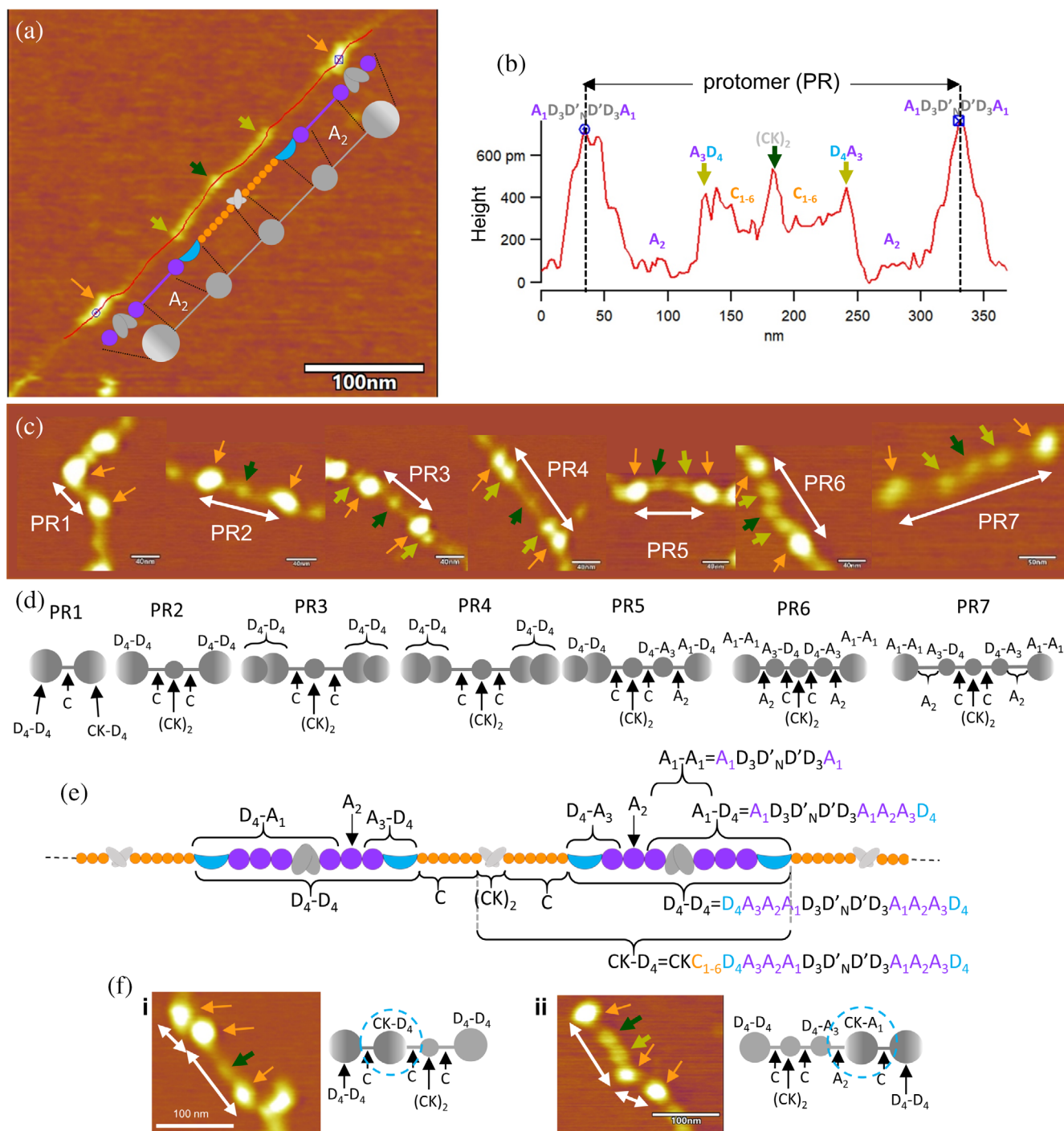
FIGURE 5 Assignment of conformational states to VWF protomers. (a) Height-contrast AFM image showing a section of an elongated VWF multimer that highlights the topographical structure of a highly extended protomer. The red line running along the axis of the multimer was drawn manually and used for measuring the height profile (shown in b). The overlaid schematics indicate the domain and nodular structure of the extended protomer. Orange arrows mark the large terminal nodules that correspond to the $A_1D_3D'D'D_3A_1$ domains in the multimer. The dark green arrow points at the central small nodule that corresponds to the $(CK)_2$ domains in the dimer. The light green arrows point at the small nodules which we interpret to correspond to the A_3D_4 domains. (b) Height profile plot measured along the axis of the protomer. Vertical dashed lines indicate the centers of the large nodules, in between which the end-to-end length of the protomer was measured. Colored arrows are identical to the ones in the AFM image, and point at the peaks of the profile plot that correspond to respective VWF domain groups labeled with the appropriate letter codes. (c) Examples of the seven groups of protomers classified according to the arrangement of the component domains. The groups are shown in order of increasing extension. Scale bars are 40 nm on PR1-PR6, and 60 nm on PR7. Arrow coloring is identical to that in (a). (d) Phenomenological models of the seven groups of protomers. Nodules that contain domains or domain groups are shown with gray circles, and interconnecting rods with gray lines. Labels are explained in (e) with the letter codes superimposed on the domain structure of the VWF multimer. C_{1-6} domains labeled with a single C. (f) Examples of protomers with asymmetric conformations

TABLE 1 Domain layout of the different VWF protomer conformers, shown graphically in Figure 5

PR1:
--(D$_4$A$_3$A$_2$A$_1$D$_3$D$'_N$**D$'$D$_3$A$_1$A$_2$A$_3$D$_4$**)--C$_{1-6}$--((CK)$_2$C$_{1-6}$**D$_4$A$_3$A$_2$A$_1$D$_3$D$'_N$**D$'$D$_3$A$_1$A$_2$A$_3$D$_4$)--
PR2:
--(D$_4$A$_3$A$_2$A$_1$D$_3$D$'_N$**D$'$D$_3$A$_1$A$_2$A$_3$D$_4$**)--C$_{1-6}$--(CK)$_2$--C$_{1-6}$--(**D$_4$A$_3$A$_2$A$_1$D$_3$D$'_N$**D$'$D$_3$A$_1$A$_2$A$_3$D$_4$)--
PR3:
--(D$_4$A$_3$A$_2$-A$_1$D$_3$D$'_N$**D$'$D$_3$A$_1$A$_2$A$_3$D$_4$**)--C$_{1-6}$--(CK)$_2$--C$_{1-6}$--(**D$_4$A$_3$A$_2$A$_1$D$_3$D$'_N$**D$'$D$_3$A$_1$-A$_2$A$_3$D$_4$)--
PR4:
--(D$_4$A$_3$A$_2$A$_1$D$_3$D$'_N$**D$'$D$_3$A$_1$-A$_2$A$_3$D$_4$**)--C$_{1-6}$--(CK)$_2$--C$_{1-6}$--(**D$_4$A$_3$A$_2$-A$_1$D$_3$D$'_N$**D$'$D$_3$A$_1$A$_2$A$_3$D$_4$)--
PR5:
--(D$_4$A$_3$A$_2$-A$_1$D$_3$D$'_N$**D$'$D$_3$A$_1$A$_2$A$_3$D$_4$**)--C$_{1-6}$--(CK)$_2$--C$_{1-6}$--(**D$_4$A$_3$**)--**A$_2$**--(**A$_1$D$_3$D$'_N$**D$'$D$_3$A$_1$A$_2$A$_3$D$_4$)—
--(D$_4$A$_3$A$_2$-A$_1$D$_3$D$'_N$**D$'$D$_3$A$_1$**)--**A$_2$**--(**A$_3$D$_4$**)--C$_{1-6}$--(CK)$_2$--C$_{1-6}$--(**D$_4$A$_3$A$_2$A$_1$D$_3$D$'_N$**D$'$D$_3$A$_1$A$_2$A$_3$D$_4$)—
PR6:
--(A$_1$D$_3$D$'_N$**D$'$D$_3$A$_1$**)--**A$_2$**--(**A$_3$D$_4$**)--C$_{1-6}$--(CK)$_2$--C$_{1-6}$--(**D$_4$A$_3$**)--**A$_2$**--(**A$_1$D$_3$D$'_N$**D$'$D$_3$A$_1$)--
PR7:
--(A$_1$D$_3$D$'_N$**D$'$D$_3$A$_1$**)---**A$_2$**---(**A$_3$D$_4$**)--C$_{1-6}$--(CK)$_2$--C$_{1-6}$--(**D$_4$A$_3$**)---**A$_2$**---(**A$_1$D$_3$D$'_N$**D$'$D$_3$A$_1$)--

Note: Domains that belong to a full dimer (in the center of each row) are shown in bold. Vicinal domains that contribute to the same single nodule are in parentheses. The number of dashes in between domain letters indicates the magnitude of the extension. PR5 domain assignment is arbitrary because the typical "large nodule—thin segment—small nodule—thin segment—small nodule—thin segment—large nodule" chain might correspond to two layouts, presented below

with random-coil structure (Figure 1d) similar to prior AFM reports (Bonazza et al., 2015; Seyfried et al., 2010). In our magnified AFM images (Figure 1e), the intrafilamentous substructure of VWF could be resolved. Nodules could be observed along the contour which were interconnected with thin, mostly straight segments. We identified the "large nodule—thin segment—small nodule—thin segment—large nodule" unit (cf. Figure 1e, gray arrowhead) as the VWF protomer (Lof et al., 2019). The large nodules bounding the protomer hence correspond to the interprotomer junction in which N-terminal nodules overlap (Fowler et al., 1985). The small central nodule corresponds to overlapping C-terminal cysteine knot (CTCK) domains interlinked via disulfide bridges. Because there are two CK domains in the central nodule, we refer to it as (CK)$_2$. In this conformation (Figure 1e, gray arrowhead), the C-domain stem is in a fully open state due to the low-calcium environment (Lof et al., 2019), therefore, the highlighted "thin segment—

small nodule—thin segment" portion of the VWF multimer corresponds to the C$_{1-6}$(CK)$_2$C$_{1-6}$ domains. Partially or completely zippered dimers could also be identified (Figure S1) (Lof, Konig, et al., 2019; Zhou et al., 2011; Zhou et al., 2012), albeit at a smaller frequency. We used AFM images collected under aqueous buffer conditions on conformationally relaxed VWF multimers to calculate their mean cross-sectional diameter (Equation (1), see Section 4). The mean diameter was 4.4 ± 1.1 nm ($N = 7$), in good agreement with earlier observations (Siedlecki et al., 1996). Altogether, even though the local protomer structure could be resolved in some relaxed VWF multimers, they were mostly contracted, resulting in unresolvable structural overlap between vicinal protomers.

To resolve protomer structure in situ in the VWF multimer and to reveal the effects of mechanical forces, the sample was exposed to a receding meniscus (Figure 2). There are multiple forces acting on the experimental system at different points of attack (Figure 2a): (1) centrifugal force (F_c) acts on the droplet and the VWF multimer; (2) drag force (F_d) emerges by the motion of the fluid past the tethered VWF multimer and acts along its length; and (3) surface-tension-based force (F_{st}) emerges as the meniscus moves along the VWF multimer and acts on its circumference. The forces acting directly on the multimer are counter-balanced by its adhesion to the substrate surface, its elasticity and intramolecular interactions (Martonfalvi & Kellermayer, 2014). As a result, the VWF multimer is captured in a stretched state that allows for the identification of structural intermediates of extension. F_c acting on the fluid droplet, calculated from Equation (4), was 1.27 N. By comparison, F_c acting directly on the VWF multimers ranged between 0.093 and 0.49 fN depending on molecular mass ($\sim$1–5 MDa). Considering that these forces are further reduced by buoyant forces, F_c acting directly on the VWF multimers can be neglected. Hence, the relevant forces that affect VWF conformation are F_d and F_{st}. The drag force (F_d), calculated from Equation (5) (see also Figures S5, S6), for a fluid velocity of 5×10^{-3} ms^{-1}, ranged between $\sim$90 and $\sim$680 pN for the multimer contour lengths in our dataset (416–3090 nm, see Figure 4c,d). F_d decays by two orders of magnitude within 1 s due to the thinning of the liquid droplet (Tskhovrebova & Trinick, 2001), therefore, the calculated forces represent the initial values during the receding meniscus experiment. Because of the length dependence of F_d, the longest VWF multimers were exposed to more than half an order greater forces than the shortest ones. The surface-tension-based force (F_{st}), calculated according to Equation (8), was 960 pN considering the average multimer diameter (4.4 nm). F_{st}, however, acts only for a very short time due to the rapid motion of the fluid (5×10^{-3} ms^{-1}). The exposure time
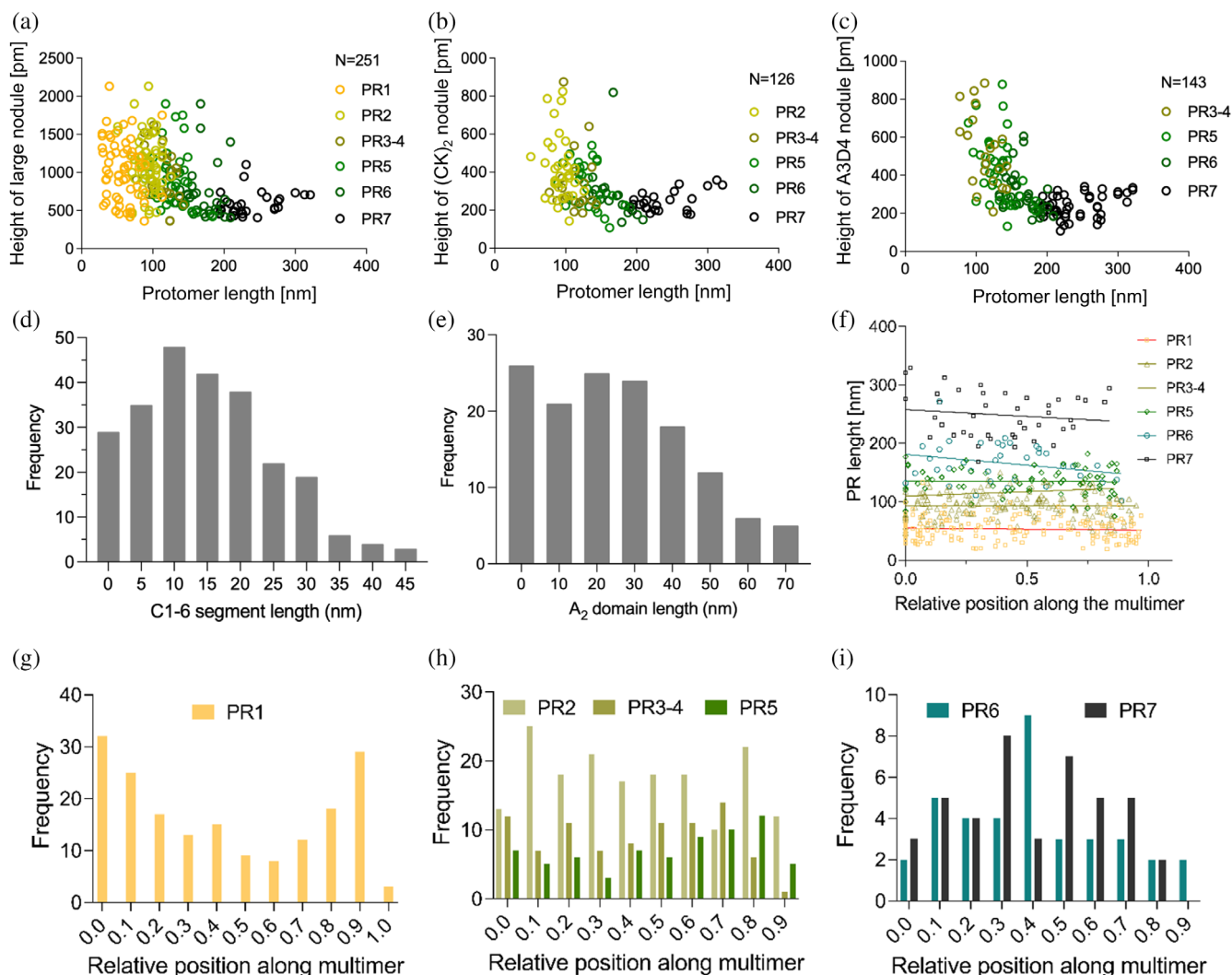
FIGURE 6 Analysis of structural parameters of VWF protomers. Topographical height of the large (a), the $(CK)_2$ (b) and the A_3D_4 (c) nodules as a function of protomer length. (d) Distribution of the C_{1-6} segment length (measured as the peak-to-peak distance between the D_4 and CK domains minus the average width of the CK domain, see Data S1) in the entire AFM dataset. (e) Distribution of the A_2 domain length (measured as the gap distance between the A_1 and A_3 domains, see Data S1) in the entire AFM dataset. (f) Length of the different protomer conformers as a function of their relative position along the multimer. Distribution of the shortest (PR1) (g) the mid-size (PR2, PR3–4, PR5) (h) and longest (PR6, PR7) (i) protomers along the VWF contour

ranged between 0.08 and 0.6 ms for the shortest (416 nm) and longest (3090 nm) multimers, respectively (Data S1). Thus, VWF multimers were exposed here to forces far exceeding the 11–21 pN considered critical to induce domain unfolding (Ying et al., 2010; Zhang, Halvorsen, et al., 2009), albeit for very short periods of time. The VWF multimers stretched with receding meniscus (Figure 2a) became oriented (Figures 2b, S3) and extended, and a periodic pattern containing mirror-symmetric fundamental elements was revealed (Figure 2c). We identified this element as the protomer, the internal structure of which was analyzed further. Upon DTT treatment (Figure 3), the pre-stretched VWF multimers became fragmented at protomer boundaries,

topographical gaps appeared between the fragments, and the filament became contracted. Notably, however, the VWF multimers remained attached to the substrate in spite of the contraction, which is likely due to attraction between the negatively charged mica and the positively charged A1 domains. The surface attachment via the A1 domain conceivably reflects VWF's propensity of anchoring to negatively charged molecules at the site of wounds (Kalagara et al., 2018). In sum, the periodic appearance along the meniscus-stretched VWF is related to the protomers which are under tension in the extended multimer; breakage of disulfide bonds leads to fragmentation, hence protomer contraction and the release of the stored elastic energy.

TABLE 2 Parameters of distinct regions in different VWF protomer conformers

	n^a	Topographical height[b] [pm]			Length[b] [nm]		
		Large (N-terminal) nodule	$(CK)_2$ nodule	A_3D_4 nodule	Protomer	C_{1-6}CK domains	A_2 domain[c]
Conformationally relaxed VWF multimers							
PR1	95	1064 ± 273	-	-	52.8 ± 21.5	-	-
PR2	37	1074 ± 237	591.9 ± 109.8	-	68.3 ± 14.6	-	-
VWF multimers stretched with molecular combing							
PR1	34	1020 ± 405	-	-	57 ± 20	-	-
PR2	36	1089 ± 359	423 ± 159	-	93 ± 14	46 ± 11	-
PR3–4	19	983 ± 324	346 ± 174	529 ± 192	113 ± 18	47 ± 10	25 ± 5
PR5	28	939 ± 387	338 ± 117	436 ± 174	131 ± 22	42 ± 11	38 ± 15
PR6	19	758 ± 364	282 ± 144	302 ± 106	167 ± 23	33 ± 7	51 ± 13
PR7	24	587 ± 156	246 ± 54	238 ± 60	240 ± 38	44 ± 9	76 ± 17

[a]n = number of analyzed protomers in 14 VWF multimers.
[b]Mean ($\pm$SD).
[c]A1–A3 peak-to-peak distance, which is related to A2 extension (see Data S1).

The extended beads-on-a-string structure of the VWF multimer allowed us to identify local structural states of protomers (Figures 4–6, S2). The contour length of multimers ranged between 416 and 3090 nm, which is comparable to prior observations (Eppell et al., 1993; Fowler et al., 1985; Marchant et al., 1992; Ohmori et al., 1982; Seyfried et al., 2010; Slayter et al., 1985); (Yokota et al., 1999). We identified the large nodules appearing periodically along the contour as the N-terminal VWF junctions, hence the section between the large nodules is the protomer itself (Figure 4a) (Fowler et al., 1985; Lof, Konig, et al., 2019; Marchant et al., 1992; Slayter et al., 1985; Zhou et al., 2012). The distance between vicinal large nodules thus reflects the end-to-end length of the protomer. Protomer length ranged between 19 and 329 nm, which is much longer than measured before either with electron microscopy (Fowler et al., 1985; Slayter et al., 1985), AFM (Bonazza et al., 2015; Marchant et al., 1992), or fluorescence microscopy (Fu et al., 2017).

Protomer length, either calculated as an average value (Figure 4c) or measured directly (Figure 4d), increased with increasing multimer contour length. Thus, the greater the VWF contour length, the more extended its protomers. The increased protomer extension can be explained by exposure to greater drag force which scales with the length of the multimer.

In AFM images of the highly extended VWF protomer (Figure 5a) details of the domain structure could be discerned, allowing us to identify seven topographical structural classes (Figures 5c,d, S2, Table 1) (PR1 to PR7) related to conformational states at progressively increasing extension. PR1 is the shortest and most contracted state, in which only the two distal large nodules

interconnected by a thin segment can be seen. Surprisingly, the characteristic central small $(CK)_2$ nodule is hidden, most likely due to its fusion with one of its vicinal large nodules (Table 1). PR2 is more extended and displays the typical "large nodule—thin segment—small nodule—thin segment—large nodule" appearance, in which the C-domain stem is in the open state.(Lof, Konig, et al., 2019) Upon advancing to the PR3 and PR4 states, structural changes and rearrangements occur in the large nodules. One of the A_2 domains in the large nodule unfolds, which results in the partitioning of the large nodule into two. Since there are two A_2 domains initially in the large nodule, as it comprises the overlapping N-terminal domains from two vicinal protomers, up to four combinations of this state may exist. PR3 and PR4 correspond to the two mirror-symmetric states out of the four (Table 1). Altogether, however, PR3 and PR4 are analogous. Upon further extension, and reaching PR5, one of the already unfolded A_2 domains becomes extended. PR5 is a quasi-symmetric state in the topographical sense, but because the $(CK)_2$ nodule is off center, the extension of the monomers within the protomer is asymmetric. In PR6, the A_2 domains of both monomers within the protomer are slightly extended. A_2 domain extension then becomes pronounced in the PR7 state. Further to the functionally asymmetric PR1 and PR5 states, we found topographically asymmetric ones as well (Figure 5f), which apparently arise due to the fusion of the $(CK)_2$ nodule with vicinal large nodules. Such asymmetry supports the idea that the mechanically independent unit of VWF is the monomer, not the protomer. (Parker & Lollar, 2021) In summary, based purely on protomer end-to-end length, the first step in VWF protomer

extension is the uncoiling of the C-domain stem (C_{1-6} segment), which is followed by the progressive unfolding of A_2 domains that leads to segmentation and rearrangement within the large N-terminal overlap nodules, and finally, a significant extension of the unfolded A_2 domains takes place (Video S1). Thus, most VWF extension occurs at the expense of C_{1-6} uncoiling and unfolded A_2 domain extension. It remains a question whether further domains unfold and extend during VWF stretch. The topographical height of all nodules decreases with increasing protomer length (Figure 6a–c). Even though dehydration-induced compaction may contribute to these changes, the results suggest that further structural changes, conceivably partial domain unfolding, may indeed take place in addition to the changes in C_{1-6} and A_2. The finding that the end-to-end length of C_{1-6} (Figure S7) extends beyond the predicted maximum of 30 nm (Figure 6d) (Mueller et al., 2016; Springer, 2014) points at possible unfolding and extension within the bounding nodules. Furthermore, a detailed analysis of unfolded A_2 domain end-to-end length (Figures S6–S8) also lends support to the idea that partial unfolding and extension may take place in the nodules bounding the unfolded A_2 domain. Further analysis of the individual domains is required to uncover the entire spectrum of subtle structural changes that occur in VWF during mechanical stretch. The unfolded A_2 domain may, in highly stretched conditions, become nearly fully extended, as its end-to-end distance almost reaches the theoretical contour length of $\sim$73 nm (Figure 6e, Table S1). A_2 length allows to estimate the entropic force in the extended domain, hence the apparent stretching force to which the VWF multimer was exposed to before stabilization during the receding meniscus experiment (Data S1). Considering the $\sim$55 nm A_2 domain length at the half maximum of the statistical frequency (Figure 6e), the apparent stretching force is 45 pN, which exceeds the threshold (11–21 pN) for A_2 unfolding (Ying et al., 2010; Zhang, Halvorsen, et al., 2009). Altogether, even though the initial mechanical conditions in the receding meniscus experiment exceed the shear stress and shear rate in physiological and pathological conditions, due to the thinning of the fluid droplet(Tskhovrebova & Trinick, 2001) the effective force that eventually determines the final VWF conformation is in the relevant range (Panteleev et al., 2021; Roux, Bougaran, Dufourcq, & Couffinhal, 2020; Wootton & Alevriadou, 2012; Wootton & Ku, 1999)

The conformers were not distributed evenly along the multimer. Rather, the contracted protomer (PR1) was more frequently found at the ends of the multimer, while the highly extended protomers (PR6, PR7) were in the middle (Figures 6g–i, S3). The centrally located overstretch of an extended object, called necking, is characteristic of plastic behavior and has been found in biomolecular systems (Sziklai et al., 2022). Although necking arises in systems held firmly at both ends, we speculate that just prior to the departure of the receding meniscus from the surface of the stretched VWF multimer, such a mechanical geometry is present, albeit for a short period of time. Interestingly, this novel finding has recently been predicted to occur in VWF by coarse-grain simulation (Morabito et al., 2018). The biological significance of the uneven protomer extension along a stretched VWF multimer is currently unknown.

In the present work, we have shown that the VWF multimer, when exposed to a variety of dynamically changing local forces, responds with a hierarchical and spatially determined series of conformational changes and local overextension. Whether and how a protein strand responds conformationally to the mechanical environment depends on the instantaneous force and the kinetics of the relevant structural changes. Given our experimental setting, we capture the final confirmation of the VWF multimer that reflects a history of exposure to high initial forces that decay to levels that are relevant for physiology and pathology. It remains a question whether VWF is conformationally equilibrated or kinetically trapped under these conditions. Nevertheless, as different ligands may bind to different VWF domains depending on conformational status, the hierarchical and uneven protomer extension may provide a spatial control of VWF-associated biochemical reactions.

4 | METHODS

4.1 | Preparation, storage, and characterization of VWF

Therapeutic concentrate (Haemate P 1200 IU/500 IU, CSL Behring, Marburg, Germany) was the source of plasma-derived VWF. VWF was separated from albumin with HiTrap Heparin HP and Desalting columns (GE Healthcare, Chicago, IL) equilibrated with 10 mM Hepes, pH 7.35. 0.5 ml fractions were eluted with 0–0.5 M NaCl gradient and stored at -80°C until further use. VWF concentration was estimated by antigen-binding (VWF:Ag) using ELISA. Multimer distribution was determined with 1% SDS-agarose electrophoresis (Figure 1c) followed by electroblotting and immunochemical staining (Cejka, 1982; Novak, Deckmyn, Damjanovich, & Harsfalvi, 2002). Fractions rich in high-molecular-weight multimers were used.

4.2 | Immobilization of VWF multimers for AFM

For immobilization of multimers in the relaxed state, 10 μl of diluted VWF (2 μg/ml final VWF:Ag in PBS, 16 mM Na_2PO_4, 4 mM $NaHPO_4$, 150 mM NaCl; pH 7.4) was pipetted on freshly cleaved mica (Highest Grade V1 Mica, $d = 12$ mm; TedPella, Redding, CA), incubated for 1 min, rinsed with MilliQ water (Merck Millipore, Burlington, MA) and dried with a gentle stream of high-purity N_2. For stretching VWF, we used molecular combing (Martonfalvi & Kellermayer, 2014). Briefly, 20 μl of VWF sample (2 μg/ml final VWF:Ag in PBS containing 50% glycerol) was pipetted on the center of a mica disk mounted in a custom-built planar centrifuge rotor (radius = 3 cm) and spun to 13,000 rpm (5685 g) for 10 s (Biofuge Pico, Heraeus, Hanau, Germany) (Figures 2a; S4). (Times required for the consecutive steps: pipetting and closing the centrifuge 5 s, acceleration 14 s, and deceleration 10 s.) Subsequently, the sample was rinsed with MilliQ water and dried with N_2. The specimens were stored in a vacuum exsiccator until imaging with AFM. All steps were carried out at $23 \pm 2°C$.

4.3 | AFM imaging

AFM images were acquired in air with a Cypher S AFM (Oxford Instruments Asylum Research, Santa Barbara, CA) in non-contact (AC) mode using silicon-nitride cantilevers (OMCL-AC160TS-R3, Olympus, Tokyo, Japan, tip radius 7 nm). Setpoint was 60–70% of the free amplitude, and typical scanning rates were 0.7 Hz. In some cases, following AFM scanning the sample was treated with dithiothreitol (DTT) to reduce disulfide bonds. 100 μl of DTT, dissolved in PBS to the desired final concentration, was pipetted on the sample. After 10 min of incubation the sample was rinsed with water and dried. Subsequently, the sample was scanned again with AFM.

4.4 | Image processing and data analysis

Images were processed with the AR16 software of the AFM (based on Igor Pro 6.34, WaveMetrics, Lake Oswego, OR). Images were corrected for flatness of field and color contrast. Width of multimers and gap distances were corrected for tip convolution as described previously (Martonfalvi & Kellermayer, 2014). Further analysis and data plotting were performed with Microsoft Excel 2016 (Microsoft, Redmond, WA) and Prism 9 (GraphPad, San Diego, CA).

4.5 | Calculation of the diameter of hydrated VWF multimer

Mean diameter of hydrated VWF multimer was calculated from AFM images acquired under aqueous buffer conditions. First, 10 μl of diluted VWF (2 μg/ml final VWF:Ag in PBS) was pipetted on freshly cleaved mica, incubated for 1 min then rinsed with MilliQ water to remove unbound material and stabilize multimers on the surface. Subsequently, 100 μl of PBS was added, and AFM imaging was carried out under aqueous buffer conditions. AFM images were corrected for flatness of field. The height (h) and the full width at half maximal height (FWHMH) of VWF multimers were measured on topographical profile plots drawn manually across the multimers. Because VWF multimers flattened on the mica surface and their cross section therefore resembled more an ellipse than a circle, VWF diameter (d) was calculated as

$$d = 2\sqrt{\frac{A}{\pi}}, \tag{1}$$

where A is the area of the ellipse calculated from the long (a) and short (b) axes of the elliptical cross section, which correspond to the half values of FWHMH and h, respectively, as

$$A = ab\pi. \tag{2}$$

4.6 | Calculation of relevant centrifugal forces

Centrifugal force (F_c) emerging in a receding meniscus experiment (Figure 2a) was calculated as

$$F_c = ma_{cp}, \tag{3}$$

where m is the mass of the accelerated object (fluid droplet or VWF multimer) and a_{cp} is centripetal acceleration that depends on the centrifugal revolutions per minute (N) and the radius (R, set by the geometry of our custom-built rotor, Figure S4) as

$$a_{cp} = 0.011N^2R. \tag{4}$$

4.7 | Calculation of drag force

The drag force (F_d) acting on a single VWF multimer stretched with receding meniscus (Figure 2a) was calculated as

$$F_d = c_{\parallel} L v, \tag{5}$$

where L is the contour length of VWF (obtained from AFM data), v is the speed of fluid flow (5×10^{-3} m s^{-1}, obtained from the shear rate at a distance of VWF radius away from the surface, see Data S1) and $c_{\parallel}$ is the drag coefficient parallel with the long axis of the multimer and can be obtained as (Howard, 2001)

$$c_{\parallel} \cong \frac{2\pi\eta}{\ln\left(2\frac{h}{r}\right)} \tag{6}$$

where η is the viscosity (7 mPas for 50% glycerol at room temperature), h is the distance from the substrate surface to the multimer axis, and r is the multimer radius. Equation (6) simplifies into

$$c_{\parallel} = 2\pi\eta \tag{7}$$

for rodlike structures near the surface (i.e., if h and r are comparable). Accordingly, the parallel drag coefficient was ~44 mPas.

4.8 | Calculation of surface-tension-based force

The force (F_{st}) acting on the VWF multimer as the meniscus of the centrifugally accelerated droplet passes along it (Figure 2a) depends on surface tension (γ) as

$$F_{st} = \gamma\pi d, \tag{8}$$

where d is the VWF diameter (Equation (1)). γ of the 50% glycerol solution used in the experiments was 69.5 pN nm^{-1}.

AUTHOR CONTRIBUTIONS

Mária Csilla Csányi: Data curation (equal); investigation (equal); methodology (equal); visualization (equal); writing – original draft (equal); writing – review and editing (equal). **Pál Salamon:** Investigation (equal); methodology (equal). **Tímea Feller:** Investigation (equal); writing – review and editing (equal). **Tamás Bozó:** Investigation (equal); writing – review and editing (equal). **Jolan Harsfalvi:** Conceptualization (equal); data curation (equal); investigation (equal); methodology (equal); project administration (equal); supervision (equal); validation (equal); writing – original draft (equal); writing – review and editing (equal). **Miklós Kellermayer:** Conceptualization (equal); funding acquisition (equal); methodology (equal); project administration (equal); supervision (equal); writing – original draft (equal); writing – review and editing (equal).

CONFLICTS OF INTEREST

The authors declare no conflicts of interest.

DATA AVAILABILITY STATEMENT

The data that support the findings of this study are available from the corresponding author upon reasonable request.

ORCID

Jolán Hársfalvi https://orcid.org/0000-0001-9940-4846
Miklós S. Z. Kellermayer https://orcid.org/0000-0002-5553-6553

REFERENCES

Baldauf C, Schneppenheim R, Stacklies W, Obser T, Pieconka A, Schneppenheim S, et al. Shear-induced unfolding activates von Willebrand factor A2 domain for proteolysis. J Thromb Haemost. 2009;7(12):2096–105.

Bonazza K, Rottensteiner H, Schrenk G, Frank J, Allmaier G, Turecek PL, et al. Shear-dependent interactions of von Willebrand factor with factor VIII and protease ADAMTS 13 demonstrated at a single molecule level by atomic force microscopy. Anal Chem. 2015;87(20):10299–305.

Cejka J. Enzyme immunoassay for factor VIII-related antigen. Clin Chem. 1982;28(6):1356–8.

Chen W, Lou J, Zhu C. Molecular dynamics simulated unfolding of von Willebrand factor a domains by force. Cellular and Molecular Bioengineering. 2009;2(1):75–86.

De Ceunynck K, Rocha S, Feys HB, De Meyer SF, Uji-i H, Deckmyn H, et al. Local elongation of endothelial cell-anchored von Willebrand factor strings precedes ADAMTS13 protein-mediated proteolysis. J Biol Chem. 2011;286(42):36361–7.

Eppell SJ, Zypman FR, Marchant RE. Probing the resolution limits and tip interactions of atomic force microscopy in the study of globular proteins. Langmuir. 1993;9(9):2281–8.

Fowler WE, Fretto LJ, Hamilton KK, Erickson HP, McKee PA. Substructure of human von Willebrand factor. J Clin Invest. 1985;76(4):1491–500.

Fu H, Jiang Y, Yang D, Scheiflinger F, Wong WP, Springer TA. Flow-induced elongation of von Willebrand factor precedes tension-dependent activation. Nat Commun. 2017;8(1):324.

Howard J. 2001. Mechanics of motor proteins and the cytoskeleton. Sinauer Associates, Publishers.

Kalagara T, Moutsis T, Yang Y, Pappelbaum KI, Farken A, Cladder-Micus L, et al. The endothelial glycocalyx anchors von

Willebrand factor fibers to the vascular endothelium. Blood Adv. 2018;2(18):2347–57.

Karampini E, Bierings R, Voorberg J. Orchestration of primary hemostasis by platelet and endothelial lysosome-related organelles. Arterioscler Thromb Vasc Biol. 2020;40(6):1441–53.

Lancellotti S, Sacco M, Basso M, Cristofaro RD. Mechanochemistry of von Willebrand factor. Biomolecular Concepts; 2019. p. 194.

Lof A, Konig G, Schneppenheim S, Schneppenheim R, Benoit M, Budde U, et al. Advancing multimer analysis of von Willebrand factor by single-molecule AFM imaging. PLoS One. 2019;14(1): e0210963.

Lof A, Walker PU, Sedlak SM, Gruber S, Obser T, Brehm MA, et al. Multiplexed protein force spectroscopy reveals equilibrium protein folding dynamics and the low-force response of von Willebrand factor. Proc Natl Acad Sci U S A. 2019;116(38):18798–807.

Marchant RE, Lea AS, Andrade JD, Bockenstedt P. Interactions of Vonwillebrand-factor on mica studies by atomic force microscopy. J Colloid Interf Sci. 1992;148(1):261–72.

Martonfalvi Z, Kellermayer M. Individual globular domains and domain unfolding visualized in overstretched titin molecules with atomic force microscopy. PLoS One. 2014;9(1):e85847.

Morabito M, Dong C, Wei W, Cheng X, Zhang XF, Oztekin A, et al. Internal tensile force and A2 domain unfolding of von Willebrand factor Multimers in shear flow. Biophys J. 2018;115(10): 1860–71.

Mueller JP, Mielke S, Löf A, Obser T, Beer C, Pippig DA, et al. Force sensing by the vascular protein Von Willebrand factor is tuned by a strong Intermonomer interaction. Biophys J. 2016; 110(3):27a.

Novak L, Deckmyn H, Damjanovich S, Harsfalvi J. Shear-dependent morphology of von Willebrand factor bound to immobilized collagen. Blood. 2002;99(6):2070–6.

Ohmori K, Fretto LJ, Harrison RL, Switzer ME, Erickson HP, McKee PA. Electron microscopy of human factor VIII/Von Willebrand glycoprotein: effect of reducing reagents on structure and function. J Cell Biol. 1982;95(2 Pt 1):632–40.

Panteleev MA, Korin N, Reesink KD, Bark DL, Cosemans J, Gardiner EE, et al. Wall shear rates in human and mouse arteries: standardization of hemodynamics for in vitro blood flow assays: communication from the ISTH SSC subcommittee on biorheology. J Thromb Haemost. 2021;19(2):588–95.

Parker ET, Lollar P. Conformation of the von Willebrand factor/factor VIII complex in quasi-static flow. J Biol Chem. 2021;296:100420.

Roux E, Bougaran P, Dufourcq P, Couffinhal T. Fluid shear stress sensing by the endothelial layer. Front Physiol. 2020;11:861.

Ruggeri ZM, Zimmerman TS. The complex multimeric composition of factor VIII/von Willebrand factor. Blood. 1981;57(6):1140–3.

Seyfried BK, Friedbacher G, Rottensteiner H, Schwarz HP, Ehrlich H, Allmaier G, et al. Comparison of plasma-derived and recombinant von Willebrand factor by atomic force microscopy. Thromb Haemost. 2010;104(3):523–30.

Shimanuki C, Matsuta Y, Fujita R, Kumaki J. Molecular combing of a flexible polymer chain by simple spin-casting. ACS Omega. 2018;3(4):3983–90.

Siedlecki CA, Lestini BJ, Kottke-Marchant KK, Eppell SJ, Wilson DL, Marchant RE. Shear-dependent changes in the three-dimensional structure of human von Willebrand factor. Blood. 1996;88(8):2939–50.

Slayter H, Loscalzo J, Bockenstedt P, Handin RI. Native conformation of human von Willebrand protein. Analysis by electron microscopy and quasi-elastic light scattering. J Biol Chem. 1985;260(14):8559–63.

Springer TA. von Willebrand factor, Jedi knight of the bloodstream. Blood. 2014;124(9):1412–25.

Sziklai D, Sallai J, Papp Z, Kellermayer D, Martonfalvi Z, Pires RH, et al. Nanosurgical manipulation of titin and its M-complex. Nanomaterials (Basel). 2022;12(2):178.

Tskhovrebova L, Trinick J. Flexibility and extensibility in the titin molecule: analysis of electron microscope data. J Mol Biol. 2001;310(4):755–71.

Wang Y, Morabito M, Zhang XF, Webb E III, Oztekin A, Cheng X. Shear-induced extensional response behaviors of tethered von Willebrand factor. Biophys J. 2019;116(11):2092–102.

Wohner N, Kovács A, Machovich R, Kolev K. Modulation of the von Willebrand factor-dependent platelet adhesion through alternative proteolytic pathways. Thromb Res. 2012;129(4): e41–6.

Wootton DM, Alevriadou BR. The shear stress of busting blood clots. N Engl J Med. 2012;367(14):1361–3.

Wootton DM, Ku DN. Fluid mechanics of vascular systems, diseases, and thrombosis. Annu Rev Biomed Eng. 1999;1:299–329.

Ying J, Ling Y, Westfield LA, Sadler JE, Shao JY. Unfolding the A2 domain of von Willebrand factor with the optical trap. Biophys J. 2010;98(8):1685–93.

Yokota H, Sunwoo J, Sarikaya M, van den Engh G, Aebersold R. Spin-stretching of DNA and protein molecules for detection by fluorescence and atomic force microscopy. Anal Chem. 1999; 71(19):4418–22.

Zhang Q, Zhou Y-F, Zhang C-Z, Zhang X, Lu C, Springer TA. Structural specializations of A2, a force-sensing domain in the ultra-large vascular protein von Willebrand factor. Proc Natl Acad Sci. 2009;106(23):9226–31.

Zhang X, Halvorsen K, Zhang CZ, Wong WP, Springer TA. Mechanoenzymatic cleavage of the ultralarge vascular protein von Willebrand factor. Science. 2009;324(5932):1330–4.

Zhou YF, Eng ET, Nishida N, Lu C, Walz T, Springer TA. A pH-regulated dimeric bouquet in the structure of von Willebrand factor. EMBO J. 2011;30(19):4098–111.

Zhou YF, Eng ET, Zhu J, Lu C, Walz T, Springer TA. Sequence and structure relationships within von Willebrand factor. Blood. 2012;120(2):449–58.

SUPPORTING INFORMATION

Additional supporting information can be found online in the Supporting Information section at the end of this article.

How to cite this article: Csányi MC, Salamon P, Feller T, Bozó T, Hársfalvi J, Kellermayer MSZ. Structural hierarchy of mechanical extensibility in human von Willebrand factor multimers. Protein Science. 2023;32(1):e4535. https://doi.org/10.1002/pro.4535